



The impact of weakly bound ^{89}Zr on preclinical studies: Non-specific accumulation in solid tumors and aspergillus infection

Severin, Gregory; Jørgensen, Jesper T.; Wiehr, Stefan ; Rolle, Anna-Maria ; Hansen, Anders Elias; Maurer, Andreas ; Hasenberg, Mike ; Pichler, Bernd ; Kjær, Andreas; Jensen, Andreas Tue Ingemann

Published in:

Nuclear Medicine and Biology

Link to article, DOI:

[10.1016/j.nucmedbio.2014.11.005](https://doi.org/10.1016/j.nucmedbio.2014.11.005)

Publication date:

2015

Document Version

Peer reviewed version

[Link back to DTU Orbit](#)

Citation (APA):

Severin, G., Jørgensen, J. T., Wiehr, S., Rolle, A.-M., Hansen, A. E., Maurer, A., ... Jensen, A. T. I. (2015). The impact of weakly bound ^{89}Zr on preclinical studies: Non-specific accumulation in solid tumors and aspergillus infection. *Nuclear Medicine and Biology*, 42(4), 360–368. <https://doi.org/10.1016/j.nucmedbio.2014.11.005>

General rights

Copyright and moral rights for the publications made accessible in the public portal are retained by the authors and/or other copyright owners and it is a condition of accessing publications that users recognise and abide by the legal requirements associated with these rights.

- Users may download and print one copy of any publication from the public portal for the purpose of private study or research.
- You may not further distribute the material or use it for any profit-making activity or commercial gain
- You may freely distribute the URL identifying the publication in the public portal

If you believe that this document breaches copyright please contact us providing details, and we will remove access to the work immediately and investigate your claim.

1 **The impact of weakly bound ⁸⁹Zr on preclinical studies: Non-specific**
2 **accumulation in solid tumors and aspergillus infection**

3

4 Gregory W Severin^{1,4}, Jesper T Jørgensen², Stefan Wiehr³, Anna-Maria Rolle³, Anders E
5 Hansen^{2,4,5}, Andreas Maurer³, Mike Hasenberg⁶, Bernd Pichler³, Andreas Kjær², and Andreas I
6 Jensen^{*1,4}

7

8 ¹ *The Hevesy Laboratory, DTU Nutech, Technical University of Denmark*

9 ² *Dept. of Clinical Physiology, Nuclear Medicine & PET, Rigshospitalet and Cluster for Molecular*
10 *Imaging, Faculty of Health Science, University of Copenhagen, Denmark*

11 ³ *Werner Siemens Imaging Center, Department for Preclinical Imaging and Radiopharmacy,*
12 *Eberhard Karls University Tübingen, Tübingen, Germany*

13 ⁴ *Center for Nanomedicine and Theranostics, Technical University of Denmark*

14 ⁵ *Department of Micro- and Nanotechnology, DTU Nanotech, Technical University of Denmark*

15 ⁶ *University Duisburg-Essen, University Hospital, Institute for Experimental Immunology and*
16 *Imaging, Essen, Germany;*

17 * Corresponding author: Technical University of Denmark, Frederiksborgvej 399, bld. 202, 4000

18 Roskilde, Denmark. Tel: +45 20126187; Fax: +45 46775347.

19 E-mail address: atiije@dtu.dk (A. Jensen)

20

21 Abbreviated title: ⁸⁹Zr accumulation in tumors and aspergillosis

22 Key words: Zr-89, PET/MR, mouse model, cancer, infection, Aspergillus fumigatus

23 **Abstract**

24 Preclinical studies involving ^{89}Zr often report significant bone accumulation, which is associated
25 with dissociation of the radiometal from the tracer. However, experiments determining the
26 uptake of unbound ^{89}Zr in disease models are not performed as routine controls. The purpose
27 of the present study was to investigate the impact of free or weakly bound ^{89}Zr on PET
28 quantifications in disease models, in order to determine if such control experiments are
29 warranted. **Methods:** Chemical studies were carried out to find a ^{89}Zr compound that would
30 solubilize the ^{89}Zr as a weak chelate, thus mimicking free or weakly bound ^{89}Zr released in
31 circulation. ^{89}Zr oxalate had the desired characteristics, and was injected into mice bearing
32 FaDu and HT29 solid tumor xenografts, and mice infected in the lungs with the mold *Aspergillus*
33 *fumigatus*, as well as in healthy controls (naïve). PET/CT and PET/MR imaging followed to
34 quantify the distribution of the radionuclide in the disease models. **Results:** ^{89}Zr oxalate was
35 found to have a plasma half-life of 5.1 ± 2.3 h, accumulating mainly in the bones of all animals.
36 Both tumor types accumulated ^{89}Zr on the order of 2-4% ID/cm³, which is comparable to EPR-
37 mediated accumulation of certain species. In the aspergillosis model, the concentration of ^{89}Zr
38 in lung tissue of the naïve animals was 6.0 ± 1.1 %ID/g. This was significantly different from that
39 of the animals with advanced disease, showing $11.6\% \pm 1.8$ %ID/g. **Conclusions:** Given the high
40 levels of ^{89}Zr accumulation in the disease sites in the present study, we recommend control
41 experiments mapping the biodistribution of free ^{89}Zr in any preclinical study employing ^{89}Zr
42 where bone uptake is observed. Aqueous ^{89}Zr oxalate appears to be a suitable compound for
43 such studies. This is especially relevant in studies where the tracer accumulation is based upon
44 passive targeting, such as EPR.

45 1. Introduction

46

47 ^{89}Zr is a popular radionuclide for the radiolabeling of monoclonal antibodies (mAbs) and similar
48 proteins for PET imaging [1–5]. However, several studies on ^{89}Zr -radiolabeled mAbs show
49 significant bone uptake of ^{89}Zr [2,6,7]. This uptake is often attributed to chelate instability, with
50 ^{89}Zr being released during the long circulation time of the mAb [2]. Alternatively, Holland et al.
51 suggested a metabolic process [8]. Regardless of the cause, the accumulation of radioactivity in
52 bones is indicative of ^{89}Zr that is no longer bound to the tracer. The presence of this unbound
53 ^{89}Zr during a PET scan can potentially have a large impact on the interpretation of results,
54 especially if it is accumulating at the disease site. In current practice however, appropriate
55 control experiments are not reported.

56

57 The biodistribution of free, or weakly chelated, ^{89}Zr was investigated in healthy mice by Abou et
58 al. using the chloride, oxalate, phosphate and citrate salts [9]. All salts were found to exhibit
59 similar biodistribution and cause accumulation of ^{89}Zr in the bones, except the phosphate,
60 which localized to liver and spleen. This was attributed to poor solubility of the ^{89}Zr phosphate.
61 Holland et al. also found the activity from the ^{89}Zr oxalate to show pronounced bone
62 accumulation, but found ^{89}Zr injected as the chloride to accumulate in the liver [8]. This was
63 also attributed to the chloride being prone to hydrolysis and poor solubility. These studies both
64 indicated that free, soluble $^{89}\text{Zr}^{4+}$ will accumulate in bone.

65

66 The nonspecific biodistribution of free ^{89}Zr in clinically relevant disease models has not been
67 investigated. However, given the large number of reports showing increased bone uptake in
68 monoclonal antibody imaging, which indicates the presence of free ^{89}Zr , knowledge of the
69 distribution of free ^{89}Zr in animal models of human disease is important. In tumors, the
70 accumulation of naked or weakly chelated radiometals, such as ^{67}Ga [10], and ^{64}Cu [11], is well
71 established. For this reason, ^{67}Ga salts have a long history of use in tumor imaging. ^{67}Ga
72 distributes via binding to transferrin [10], and it is reasonable to suspect that the same pathway
73 might be available for Zr^{4+} , or ZrO^{2+} [12]. Accordingly, free ^{89}Zr could show nonspecific tumor
74 accumulation through this pathway, which might disturb the correct interpretation of
75 accumulation data from mAb imaging. In addition, enhanced permeation and retention (EPR)
76 dominated localization after metal association with endogenous serum proteins, such as
77 albumin, may give rise to lesion uptake of free ^{89}Zr [13,14]. As nanoparticles are typically
78 thought to localize to tumors via EPR [15], the presence of free ^{89}Zr may have consequences for
79 the interpretation of tumor accumulation data for ^{89}Zr -labeled nanoparticles.

80

81 ^{89}Zr -labeled antibodies are not only in use for tumor imaging, but are also being investigated for
82 the diagnosis of other diseases such as pulmonary aspergillosis. In *Aspergillus fumigatus*
83 infections, an extracellular siderophore is excreted by the mold [16]. This was recently utilized
84 by Petrik et al. in preclinical PET studies with ^{68}Ga labeled siderophores TAFC and FSC [17,18].
85 These chelators exhibit multiple hydroxamate groups, similar to the most successful ^{89}Zr
86 chelator desferrioxamine B, which itself is a siderophore produced by streptomyces bacteria
87 [19]. Such extracellular siderophores may take up free or weakly bound ^{89}Zr and facilitate its

88 accumulation in *Aspergillus* infected tissues. This accumulation, coupled with the EPR-mediated
89 accumulation occurring as a result of inflammation and transferrin-receptor upregulation, could
90 give a very significant PET signal from lung accumulation of free or weakly bound ^{89}Zr in
91 circulation in pulmonary aspergillosis. Therefore, knowledge of the biodistribution of free ^{89}Zr
92 in solid tumors as well as in other disease sites, such as *A. fumigatus* infected tissues, is crucial
93 before initiating a preclinical positron emission tomography (PET) study with ^{89}Zr .

94

95 The aim of this work was to investigate the biodistribution of weakly chelated ^{89}Zr in relevant
96 murine disease models compared to their healthy controls. We set out to determine whether 1)
97 free ^{89}Zr exhibits accumulation in FaDu and HT29 tumor xenografts in mice and 2) whether
98 biodistribution, especially in lungs, is significantly different between healthy animals and those
99 with pulmonary aspergillosis. Further, the criteria for the injected ^{89}Zr to be considered 'free',
100 was that it was stable in solution and able to interact and associate with complexing molecules
101 and other blood stream components. For this reason we also investigated a range of
102 complexing ligands for their ability to restrict hydrolysis of ^{89}Zr and allow chelation by
103 *diethylene triamine pentaacetic acid* (DTPA).

104

105 2. Materials and Methods

106

107 2.1. Materials

108 Yttrium foils were purchased from Alfa Aesar. All solvents and chemicals were purchased from
109 Sigma Aldrich. ^{89}Zr was produced on a GE PETtrace Cyclotron. Radio-TLC was performed on a
110 Raytest MiniGita Star. All TLC analyses were performed on silica gel 60 F₂₅₄ plates (Merck) with
111 5% (w/v) NH₄OAc in H₂O-MeOH (1:1) as eluent, in which the R_f of ^{89}Zr -DTPA is 0.7 and $^{89}\text{Zr}^{4+}$
112 does not elute. Radioactivity was measured using a Veenstra Instruments dose calibrator VDC-
113 505. QMA cartridges were from Waters. Osmolalities were measured on an Osmomat 030
114 cryoscopic osmometer (Gonotec). pH was measured on an Inolab 740 electronic pH-meter
115 (WTW). Radionuclidic purity was measured on an LGC-5 high purity germanium detector
116 (Princeton Gamma-Tech). Metal ions were quantified with an ICAP 7000 ICP-OES (Thermo
117 Scientific). Ultrapure water was used in all cases (Milli-Q water purification system, Millipore).

118

119 ^{89}Zr chloride was prepared according to the method of Holland *et al.* [20]. In brief, natural 660
120 μm thick yttrium foils, were irradiated with 15 μA of protons degraded from 16 MeV to 11 MeV
121 with an 800 μm aluminum plate. The produced $^{89}\text{Zr}^{4+}$ was separated from the yttrium target
122 after digestion in aqueous HCl (3 mL, 6 M) by trapping on hydroxamate resin (50-100 mg),
123 followed by elution of the $^{89}\text{Zr}^{4+}$ in aqueous oxalic acid (3 mL, 1 M). A quarternary methyl
124 ammonium Sep-Pak cartridge (QMA light, Waters) was used to trap the anionic ^{89}Zr oxalate
125 complex from the oxalic acid solution, and after washing with ultrapure water (30 mL), the ^{89}Zr

126 was released in aqueous HCl (200 μ L, 2 M). This solution was taken to dryness under argon flow
127 at 110 $^{\circ}$ C for 15 minutes, furnishing ^{89}Zr chloride.

128

129 **2.2. Comparison of aqueous solutions for injection of 'free' ^{89}Zr**

130 The following experiments were performed to test the ability of various complexing ligands to
131 restrict hydrolysis of ^{89}Zr and allow chelation by DTPA. To vials containing dry ^{89}Zr chloride was
132 added 1.3 mL of either 1) saline, 2) 10 mM oxalic acid in saline at pH \approx 5.5, 3) 10 mM oxalic acid
133 in saline at pH \approx 7.0, 4) 10 mM citric acid in saline at pH 5.5, 5) 10 mM citric acid in saline at pH
134 7.0, 6) neat ultrapure water, 7) isotonic sucrose solution at 924 mg/mL, 8) 10 mM sodium
135 acetate at pH 5.5 or 9) 10 mM sodium acetate at pH \approx 7.0. Each preparation was stirred for 10
136 minutes at 37 $^{\circ}$ C after which 300 μ L was removed for pH measurement. In addition, the
137 radioactivity in the total volume (1.3 mL) as well as in the removed 300 μ L was measured. To
138 the remaining 1.00 mL was then added aqueous DTPA (50 μ L, 50 mM) that had been adjusted
139 to pH 5.5 or pH 7.0, whichever was closest to the pH of the receiving ^{89}Zr -mixture. To the saline
140 (chloride), water and sucrose mixtures was added DTPA at pH 5.5. The solutions were then
141 stirred at 37 $^{\circ}$ C and monitored by radio-TLC with samples removed at t = 0 (before addition of
142 DTPA), t = 10 min, t = 30 min and t = 60 min. Each mixture was prepared and analyzed in
143 triplicate.

144

145 **2.3 Preparation and characterization of the ^{89}Zr oxalate for *in vivo* use**

146 Based on the stability and exchange experiments described above, an oxalate solution was
147 chosen for *in vivo* use. This was prepared by adding a solution of 10 mM oxalic acid in isotonic

148 saline (pH adjusted to 6.7 with NaOH) to the dried ⁸⁹Zr chloride. In order to confirm that the
149 ⁸⁹Zr was fully dissolved, a sample of the solution was removed and its activity concentration
150 was compared to the remaining fraction. Osmolality and pH were measured, and HPGE gamma
151 spectroscopy was used to determine the radionuclidic purity. ICP-OES, calibrated against Fe, Zr,
152 Zn, Cu, Ag, and Ni standards in 1% (w/v) HCl, was used to quantify metal impurities.
153 Additionally, 300 µl of the ⁸⁹Zr oxalate solution was removed and mixed with aqueous DTPA (15
154 µL, 50mM, pH 7.0). After stirring at 37 °C for 30 min, it was analyzed by radio-TLC along with a
155 sample to which no DTPA had been added. After the completion of these tests, the solution
156 was ready for injection in the animal studies.

157

158 ***2.4 In vivo studies on tumor-bearing mice***

159 The studies on tumor-bearing mice were approved by the Danish Animal Welfare Council,
160 Ministry of Justice. Human head and neck cancer cell line, FaDu and human colorectal cancer
161 cell line, HT29 (purchased from ATCC) were cultured in MEM medium with Earle's salts and
162 McCoy's 5A medium, respectively (both from Sigma-Aldrich); with 10% fetal calf serum, and
163 100 units/mL penicillin and 100 µg/mL streptomycin (Invitrogen) at 37 °C in 5% CO₂. In addition
164 the MEM medium was supplemented with 1% MEM non-essential amino acids solution (100x),
165 1 mM sodium pyruvate (both from Invitrogen) and 2 mM L-glutamine (Sigma-Aldrich). Tumors
166 were established in the left and right flank of seven-week old female NMRI nude mice (Taconic
167 Europe) by subcutaneous injection of 10⁶ cancer cells dissolved in 200 µL of a 1:1 mixture of
168 MatrigelTM (BD-Biosciences) and growth medium and were allowed to grow for 2-3 weeks for
169 tumor volumes of 50-500 mm³. Animals had access to chow and water ad libitum. For tracer

170 administration and during scans, the mice were placed in a nose cone and breathed gas
171 anesthesia (2.5% Sevoflurane (Abbot Scandinavia) mixed with 35% O₂ in N₂). A heating pad was
172 used to keep the body temperature stable. ⁸⁹Zr oxalate solution (100 μL, 9-15 MBq) was
173 injected into the tail vein of mice bearing FaDu (n = 3) and HT29 tumor xenografts (n = 4). Ten
174 minute static scans were performed on a small animal PET scanner (microPET 120, Siemens
175 Medical Solutions) at 1 h, 6 h, 20 h, 45 h, and 68 h post injection with an energy window 350-
176 650 keV and 6 ns time resolution. Each PET scan was followed by seven minutes small animal CT
177 scans (MicroCAT II Tomograph; Siemens Medical Solutions) with tube voltage and tube current
178 set at 70 kVp and 500 μA, respectively and an exposure time of 310 ms per projection (360°;
179 360 projections). Listmode data from PET acquisitions were post-processed into sinograms and
180 reconstructed using the maximum a posteriori (MAP) algorithm. Images had a resolution of 1.2
181 mm at the center field of view. PET and CT images were fused using Inveon software (Siemens
182 Medical Solutions), ROIs were drawn on different target tissue and uptake quantified as %
183 injected dose per cubic centimeter (%ID/cm³). Additionally, the tumor-to-muscle (T/M) and
184 tumor-to-blood (T/B) ratios were calculated. From the images it was evident that the
185 myocardium did not accumulate high levels of ⁸⁹Zr oxalate. As it is impossible to delineate the
186 left ventricle of the mice based on CT scans without contrast, a ROI created on the heart was
187 used for T/B-ratio and blood-circulation half-life calculations.

188

189 ***2.5 In vivo studies on A. fumigatus infected and naïve mice***

190 The studies on *A. fumigatus* infected and disease-free control mice (“naïve”) were performed
191 according to the German Animal Protection Law with permission from the responsible local

192 authorities. Infections were performed as described by Bruns *et al* [21]. Briefly, eight-week old
193 female C57BL/6 mice (Harlan Laboratories) were rendered neutropenic by an intraperitoneal
194 injection of 100 μ L anti-Gr-1 antibody solution (clone RB6-8C5 at a concentration of 1 mg/mL,
195 BioXCell). 24 h later a pulmonary *A. fumigatus* infection was induced by an intratracheal
196 application of 4×10^6 resting *A. fumigatus* spores (strain ATCC 46645), suspended in 100 μ L
197 sterile tap water. For this step the animals were anaesthetized by an intraperitoneal injection of
198 100 μ L Ketamin/Rompun solution (Ketamin: 80 mg/kg, Ratiopharm GmbH, Ulm, Germany;
199 Rompun: 15 mg/kg, Bayer HealthCare, Leverkusen, Germany). After reaching deep narcosis, the
200 animals were intubated using a 22G indwelling venous catheter (Vasofix Braunüle, B. Braun AG,
201 Melsungen, Germany) and subsequently the spore suspension was applied. To achieve a better
202 distribution of the spore mass and to avoid suffocation the animals were ventilated for one
203 minute with a small animal respirator (MiniVent, Hugo Sachs, March-Hugstetten, Germany) at a
204 rate of 250 breaths per minute at an inhalation volume of 300 μ L per breath. Animals had
205 access to food and water ad libitum.

206
207 ^{89}Zr oxalate solution (50 μ L, 10-12 MBq), was injected via the lateral tail vein. During imaging,
208 the animals were anesthetized with 1.5% isoflurane mixed with 100% oxygen. Anesthesia was
209 monitored by measuring the respiratory frequency, and the body temperature was kept at 37°C
210 by a heating pad. All mice were imaged using a small animal PET scanner (Inveon, Siemens
211 Preclinical Solutions), yielding a spatial resolution of approximately 1.3 mm. PET data were
212 acquired in list-mode, histogrammed in one 10 min time frame for the static scans and
213 reconstructed using an iterative ordered subset expectation maximization (OSEM) algorithm.

214 No attenuation correction was applied. Magnetic resonance (MR) imaging was performed on a
215 7 T small animal MR tomograph (Clinscan, Bruker Biospin MRI) obtaining anatomical
216 information for optimized organ delineation. A T2-weighted 3D space sequence (TE / TR 202 /
217 2500 ms, image matrix of 137 x 320, slice thickness 0.27 mm) was used for whole-body imaging.
218 PET images were normalized to each other, subsequently fused to the respective MR images
219 and analyzed using Inveon Research Workplace software (Siemens Preclinical Solutions).
220 Results are expressed as percentage of the injected dose per cm³ (%ID/cm³). After the last PET
221 scan, the animals were sacrificed by cervical dislocation under deep anesthesia and dissected.
222 Organs were removed, weighed and measured with an aliquot of injected solution in the γ -
223 counter (Wizard single-detector γ -counter; Perkin Elmer) using an energy window between 350
224 and 650 keV.

225
226 The *A. fumigatus* infected mice were divided into two different groups. The first group (n = 5),
227 termed “nascent disease”, received the tracer injection immediately after infection. These
228 animals, along with neutropenic uninfected controls (n = 5), “naïve”, mice were imaged with 10
229 min PET scans, followed by MR imaging, performed at 3, 24 and 48 h post-injection of the
230 tracers. In the second group (n = 4), termed “advanced disease”, infected mice were injected
231 with ⁸⁹Zr oxalate 21 hours after infection. This cohort, along with four naïve control animals,
232 was imaged 3 h after tracer injection, followed immediately by *ex vivo* biodistribution.

233

234 **2.6 Statistical Analysis**

235 Statistical analysis was performed using a two-tailed t-test. Data were considered statistically
236 significant for $p < 0.05$. All quantitative results are shown as the mean \pm 1 standard deviation
237 (SD).

238

239 **3. Results**

240

241 **3.1 Comparison of aqueous solutions for injection of 'free' ⁸⁹Zr**

242 The results from the tests on the various ⁸⁹Zr-mixtures are presented in **table 1** (pH values for
243 the mixtures) and **figures 1A** (transferability/dissolution) and **1B** (transchelation to DTPA). For
244 the pH measurements in general, the solutions with low buffer capacity at their respective pH
245 values became slightly more acidic after mixing with the dried ⁸⁹Zr activity. This was likely due
246 to leftover oxalic acid residue from the chemical separation. Our lowest water pH measurement
247 was pH = 4.65, which indicates that oxalic acid concentration was less than 13 μM (see
248 **supplemental materials** for calculation). According to the work of Kobayashi *et al.* [22], Zr⁴⁺ is
249 present as the insoluble hydroxide complex at such low oxalate concentrations. This was
250 reflected by our transferability tests (**figure 1A**). In solutions with an efficient complexing agent
251 in sufficient concentration to restrict hydrolysis, such as oxalate, citrate, or sucrose, ⁸⁹Zr was
252 readily taken into the aqueous phase, whereas hydrolysis-prone mixtures, such as water,
253 acetate, and chloride, resulted in incomplete dissolution of the ⁸⁹Zr.

254

255 Despite the fact that several solutions were able to bring ⁸⁹Zr into the aqueous environment, it
256 remained necessary to test whether the ⁸⁹Zr was still able to transchelate to DTPA. This would
257 ensure that the ⁸⁹Zr was not merely suspended as a colloid, and that the complexes in question
258 could easily transfer the radioactivity to other agents. All complexes were tested for
259 transchelation to DTPA, but only the ones with superior transferability are shown in **figure 1B**.
260 For the remainder, please refer to **supplemental materials**. Both oxalate mixtures showed fast

261 and efficient transchelation to DTPA, within 10 minutes. On the other hand, the uptake from
262 the citrate was markedly slower, showing a gradual ascent, reaching about 70-80% after one
263 hour. DTPA chelation from the sucrose was faster than from the citrate, but slower than from
264 the oxalate.

265
266 Based on the results described above, we decided to use the oxalate complex for *in vivo*
267 studies, while keeping the pH below 7. The main reason for choosing oxalate over citrate was
268 that we desired a complex with a higher propensity for transferring ^{89}Zr to other chelating
269 agents present in serum. This was expected to prevent fast renal clearance of the charged
270 complexes and to better mirror the *in vivo* situation where weakly bound ^{89}Zr is released and
271 presumably bound to endogenous serum components.

272

273 ***3.2 Preparation and characterization of the ^{89}Zr oxalate solution for *in vivo* use***

274 The results of the quality control analyses for the injected ^{89}Zr oxalate solutions were consistent
275 with those observed in the transferability/solubility and transchelation tests described above.
276 The transferability of activity in the ^{89}Zr oxalate *in vivo* formulation was 95%, indicating that the
277 ^{89}Zr was properly dissolved. The pH value was in the range of 5.5-6.7, which due to the low
278 buffer capacity of the solution was expected to fluctuate. The osmolality was 310 mOsmol/kg,
279 and was appropriate for injection (serum osmolality: 282 - 295 mOsmol/kg). Analysis by ICP-
280 OES showed both non-radioactive Zr and Fe to each be present in concentrations on the order
281 of 200 ppb. This gave specific activities against total Zr and Fe of 20-35 GBq/ μmol at time of
282 injection. Analysis by gamma spectroscopy showed only peaks originating from ^{89}Zr , indicating

283 radionuclidic purity over 99%. Analysis of the ^{89}Zr oxalate solution by radio-TLC showed that
284 >99% of the activity stayed at the origin. Following addition of DTPA, 98% of the activity shifted
285 to the Zr-DTPA peak after 30 minutes (93% after 10 minutes). This confirmed a radiochemical
286 purity of >95%, and that the activity was freely transchelated from the oxalate complex to other
287 chemical species.

288

289 **3.3 In vivo data from tumor-bearing mice**

290 Representative PET/CT images from the FaDu and HT29 tumor-bearing animals are given in
291 **Figure 2**, with organs denoted. Tumor contrast is clearly seen at both 1 h and 45 h. However, 45
292 h images are dominated by high bone accumulation.

293

294 Quantifications of the PET data are given in **Table 2**. Both tumor types showed significant
295 uptake of 2-4% ID/cm³ over the course of the study. As expected, bone uptake was prominent,
296 reaching a maximum at 20 h, followed by a plateau at around 13% ID/cm³. The tumor-to-
297 muscle (T/M) and tumor-to-blood (T/B) ratios in each tumor model are displayed in **Figure 3**.
298 The T/M values ranged from 1.5-3.7 at all time-points, reflecting the contrast observed in
299 **Figure 2**. The long circulation time of the ^{89}Zr oxalate is evident in the heart ROI data. To obtain
300 the clearance half-life, the heart ROI time activity curve for each animal was fitted with an
301 exponential function (unweighted least squares fit with constant background). The average (± 1
302 SD) blood clearance half-life was 5.1 ± 2.3 h ($n = 7$) (refer to **supplemental materials** for
303 calculation).

304

305 **3.4 In vivo data from *Aspergillus*-infected mice and healthy controls**

306 The mice infected with *A. fumigatus* were divided into two groups. In the nascent disease
307 group, where animals received the tracer injection immediately after they had been infected,
308 and their naïve controls, the PET and biodistribution data were independent of disease status
309 **(Figure 4A-D)**. Quantification of the PET results revealed enhanced uptake of ^{89}Zr in the spine
310 **(Figure 4C)** without significant differences between the tested groups. The bone uptake pattern
311 is evident by qualitative observation in the 48 h maximum intensity projection (MIP) images in
312 **Figure 4E**. The mean tracer uptake in the spine of naïve mice increased from $7.5 \pm 0.9 \text{ \%ID/cm}^3$
313 at 3 h to $18.6 \pm 1.0 \text{ \%ID/cm}^3$ at 24 h, and in infected animals from $7.5 \pm 0.3 \text{ \%ID/cm}^3$ at 3 h to
314 $16.5 \pm 1.6 \text{ \%ID/cm}^3$ at 24 h after tracer injection, further reflecting the similarity between
315 infected and naïve animals.

316
317 Contrastingly, for the group of animals with advanced disease, those infected with *A. fumigatus*
318 21 hours prior to tracer injection, the biodistributions were markedly different from the healthy
319 controls. Static PET images at 3 hours post injection **(Figure 5)** revealed significantly higher
320 uptake of ^{89}Zr ($7.8 \pm 1.3 \text{ \%ID/cm}^3$) in the lungs of *A. fumigatus* infected animals compared to the
321 naïve group ($5.7 \pm 0.3 \text{ \%ID/cm}^3$; $p = 0.048$, **Figure 6**) In addition, the uptake of ^{89}Zr in the spine
322 of naïve animals was significantly higher ($6.5 \pm 0.7 \text{ \%ID/cm}^3$) compared to the infected group
323 ($4.8 \pm 0.3 \text{ \%ID/cm}^3$; $p = 0.0088$, **Figure 6**). No significant differences were seen in liver and
324 muscle tissues **(Figure 6)**.

325

326

327 The *ex vivo* biodistribution from the advanced disease group confirmed the quantification
328 obtained from the PET imaging (**Table 3**). The data from all animals revealed high
329 concentrations of ⁸⁹Zr in the bones, blood, and highly blood-perfused organs such as the heart.
330 The %ID/g values of the blood were 10.5 ± 2.7 (naïve animals) and 8.6 ± 2.8 (advanced disease).
331 The *ex vivo* biodistribution confirmed the significant differences in the lung (p = 0.002) and
332 spine (p = 0.045) uptake between the infected and naïve animals observed with *in vivo* PET
333 quantification.

334

335

336

337

338

339

340

341

342

343

344

345

346

347 **4 Discussion**

348

349 ^{89}Zr has a half-life of 3.27 days and is therefore a useful radionuclide for elucidating the
350 biodistribution of long-circulating, biologically relevant molecules, such as antibodies and
351 nanoparticles. Currently, it is one of the most widely used nuclides for PET imaging at time-
352 points beyond two days post-injection. It allows researchers to understand how a labeled
353 molecule distributes, giving useful information that leads to better drug and tracer
354 development.

355

356 The weakness in the current practice is that the derived images quantify the distribution of the
357 radionuclide and not necessarily the intact tracer. In general this is a well-understood
358 phenomenon in PET that can be controlled for by metabolite analysis. However, in ^{89}Zr imaging
359 the problem is rarely addressed. This is surprising because in a large number of pre-clinical
360 studies involving ^{89}Zr there is heightened bone accumulation in the animals. Such high skeletal
361 uptake is indicative of ^{89}Zr that is no longer bound to the molecule of interest, but is free or
362 weakly coordinated. Given that there is an observed separation between radionuclide and the
363 traced molecule, it is important to understand how the free radionuclide is affecting the PET
364 data.

365

366 In PET imaging of antibodies ^{89}Zr is usually located in the desferrioxamine (Df) chelator. Within
367 Df, it is present as $^{89}\text{Zr}^{4+}$, with water taking up the remaining coordination sites rather than =O
368 or -OH [8]. This incomplete occupation of the first coordination shell by Df has been pointed to

369 as a chink in the armor of an otherwise incredibly stable chelate, and a possible cause for
370 release of free ^{89}Zr in preclinical studies [23]. Another reason for the presence of free ^{89}Zr in
371 mAb studies is non-specific binding of the radiometal to the protein. Often, radiolabeling is
372 reported with less than 100% yield [6,7], which means either that Df-chelation sites were in
373 shortage or that the reaction had not run to completion. In such cases surplus ^{89}Zr will be
374 present in the reaction mixture and it is reasonable to assume that some of it could bind non-
375 specifically to certain proteins. Finally, it is possible that free ^{89}Zr arises from metabolism of the
376 radiolabeled entities.

377
378 Regardless of the mechanism by which ^{89}Zr is released to the circulation, we sought a tracer
379 that would solubilize and efficiently disperse the ^{89}Zr while restricting irreversible hydrolysis.
380 We found that a solution of the radioactivity in 10 mM oxalate in isotonic saline with a pH of
381 5.0-6.5 adequately provided the desired properties. This was shown by the high solubility of the
382 ^{89}Zr in the mixture and its rapid chelation by DTPA. In addition, the *in vivo* results showed
383 limited liver accumulation. This is consistent with results reported by Abou et al. and by Holland
384 et al. where ^{89}Zr oxalate was not accumulating in the liver of healthy animals [8,9]. On this
385 basis, we conclude that our injected ^{89}Zr was adequately dissolved. Also, the plasma half-life of
386 our injected activity was 5.1 ± 2.3 h. Usually, small molecular, exogenous, highly charged
387 species, such as ^{89}Zr oxalate, can be expected to undergo fast renal clearance, as is the case
388 with free ^{89}Zr -Df [8]. For this very reason, the short circulation time of ^{89}Zr -Df makes it unsuited
389 as a tracer for monitoring the biodistribution of weakly bound ^{89}Zr . That the injected
390 radioactivity in our studies showed prolonged retention in blood suggests that either the

391 activity is shifted to other endogenous carriers with long circulation, or that the ^{89}Zr oxalate
392 itself is long-circulating. In both cases, since the oxalate is a weak complex, the long circulatory
393 property of the activity is beneficial to its distribution *via* the routes that could be expected of
394 ^{89}Zr weakly bound to long-circulating species, such as antibodies or nanoparticles.

395
396 Our initial screening of ^{89}Zr formulations revealed chloride (as saline) to inadequately prevent
397 hydrolysis and keep ^{89}Zr in solution, for which reason we deemed it unfit for *in vivo* use without
398 an additional complexing ion. This agreed with the studies performed by Holland et al., where
399 the chloride formulation was found to exhibit heavy liver accumulation [8]. In contrast, Abou et
400 al. found the chloride (as saline) to distribute similarly to otherwise free ^{89}Zr , with activity
401 mainly localizing to bones [9]. Accordingly, there is a discrepancy between the results of these
402 groups with regards to the chloride. Our study primarily supports the results for the chloride
403 achieved by Holland et al. It is possible that traces of oxalic acid remaining after preparation of
404 the chloride could aid in the solubilization and unrestricted biodistribution of ^{89}Zr present in an
405 otherwise chloride containing mixture. It should be noted that we employed the same method
406 for preparing the ^{89}Zr chloride as Holland et al., and therefore we could be expected to observe
407 the same insolubility [8].

408
409 ^{89}Zr that is released *in vivo* has the opportunity of being taken up by endogenous binding
410 agents. Likely candidates for such binding include transferrin (Tf) and albumin. Transferrin
411 labeled with ^{89}Zr through Df has been shown to accumulate in tumors and inflammations, due
412 to the upregulation of transferrin receptors as part of an inflammatory response [24,25].

413 However, binding of ^{89}Zr to the endogenous ferric binding site of transferrin without the use of
414 a chelator was found to be less suitable for *in vivo* use by Holland *et al.* [24]. The conclusion
415 that endogenous labeling was not viable as a method for producing stable $^{89}\text{Zr-Tf}$ for *in vivo*
416 imaging does not exclude the possibility of *in vivo* ^{89}Zr transport via transferrin. The somewhat
417 analogous labeling of transferrin by ^{45}Ti , and its subsequent reported localization to tumors,
418 indicates that tumor accumulation of hard, oxophilic radiometals can be due to binding to
419 transferrin [26]. The results from the HT29 and FaDu tumor models presented here do not
420 show the striking contrast (14.9 %ID/cm³ tumor accumulation at 24 h) observed by Vavere *et al.*
421 for ^{45}Ti -transferrin; albeit the difference could be attributed to the different affinities of
422 transferrin toward the metals. However, the range of the tumor accumulations we observed
423 are consistent with uptake based upon EPR, such as that of radiolabeled nanoparticles, which is
424 usually in the range of 3-6 %ID/cm³ [27–29]. Albumin may be a vehicle for tumor accumulation
425 of certain species such as radiometals or their hydroxides/oxides due to its metal binding
426 capabilities [13]. Albumin has been labeled with ^{89}Zr through desferrioxamine and gave a
427 biodistribution in tumor-bearing animals that was dominated by EPR-mediated tumor
428 accumulation, with tumor values of 2-5 %ID/cm³ measured until 20 h post injection [14]. While
429 the level of tumor accumulation (2-4% ID/cm³) observed in the present study is negligible with
430 respect to signals observed with many highly specific mAbs (*eg.* J591-PSMA in LnCaP
431 xenografts, 34-46 %ID/cm³, [8]), it is not small compared to the uptakes expected in non-
432 targeted nanoparticle imaging. Therefore, as ^{89}Zr becomes more prevalent in nanoparticle
433 imaging, differentiating between the non-specific accumulation of free ^{89}Zr , versus that of the
434 nanoparticles, must be taken into account.

435

436 As a further point, it should be noted that the impact of non-specific accumulation of free ^{89}Zr
437 in spontaneous human cancers is unknown. If free ^{89}Zr exhibits tumor accumulation due to the
438 EPR effect, translation from mice to humans may amplify the significance of non-specific
439 uptake, especially in the case of imaging with ^{89}Zr -labeled mAbs. When imaging EPR-localizing
440 agents, an increased tumor accumulation relative to total body mass from mice to humans is
441 typically seen. Harrington et al. investigated ^{111}In -labeled liposomes and found tumor uptakes
442 in mice ranging from 1-6 %ID/g over several days post-injection in an HNSCC-derived xenograft
443 model [30]. In humans, they found a tumor uptake of 33 ± 16 %ID/kg at 72 hours [31]. On the
444 contrary, targeted mAb imaging with U36 against HNX-OE (HNSCC-derived) xenografts in mice
445 gave a striking uptake of 26 ± 2 %ID/g at 144 hours[32], whereas the same mAb in humans with
446 HNSCC had an average uptake of 19 %ID/kg[33]. From these data, it is apparent that uptake in
447 man versus mouse is not directly scalable, but can depend on the mode of accumulation.
448 Accordingly, we propose that if ^{89}Zr localizes to tumors by transferrin binding and EPR uptake,
449 the impact on proper assessment of tumor uptake may be greater in humans when imaging
450 antibodies that primarily localize by active targeting.

451

452 Finally, turning to the pulmonary aspergillosis model, the results illustrate that when imaging
453 animals with advanced disease, the presence of free ^{89}Zr cannot be neglected. This disease
454 model was expected to give an uptake of free ^{89}Zr that was significantly different from naïve
455 animals for several reasons. First, as the disease progresses the lung tissue becomes highly
456 perfused, thereby giving a higher PET signal due to blood volume in the ROI, and due to EPR

457 localization. Second, the inflammation in the lungs would lead to an upregulation of the Tf-
458 receptor causing accumulation of ^{89}Zr that might have been associated with transferrin *in vivo*.
459 And lastly, higher uptake was expected due to the presence of cyclic hydroxamate-based
460 chelates in the extracellular environment of the fungus. The results of the present study do not
461 weigh in on which of these probable causes are responsible, yet they do set a benchmark for
462 significance when attempting targeted approaches to pulmonary aspergillosis imaging.

463

464 **5 Conclusions**

465

466 In this study we have shown that free ^{89}Zr , in the form of ^{89}Zr oxalate in saline, can exhibit
467 substantial tumor accumulation as well as significant accumulation in *Aspergillus* infected lungs
468 as compared to healthy lungs. Our results underline the importance of making sure that no free
469 ^{89}Zr is present when conducting ^{89}Zr PET imaging, especially in cancers and pulmonary
470 aspergillosis, as observed accumulation of radioactivity may be non-specific. In addition, our
471 results indicate that injection of free ^{89}Zr , preferably as an oxalate at $\text{pH} < 7$, should routinely be
472 performed as a control experiment to a preclinical study.

473

474 **6 Acknowledgements**

475

476 This research was supported by the EU grant FP7 MATHIAS project, the Danish Cancer Society,
477 the Lundbeck Foundation, the Novo Nordisk Foundation, Innovationsfonden, the Svend
478 Andersen Foundation and the Arvid Nilsson Foundation.

479

480 **7 References**

- 481 [1] Vugts DJ, Visser GWM, van Dongen GAMS. ^{89}Zr -PET radiochemistry in the development
482 and application of therapeutic monoclonal antibodies and other biologicals. *Curr Top*
483 *Med Chem* 2013;13:446–57.
- 484 [2] Fischer G, Seibold U, Schirmacher R, Wängler B, Wängler C. ^{89}Zr , a radiometal nuclide
485 with high potential for molecular imaging with PET: chemistry, applications and
486 remaining challenges. *Molecules* 2013;18:6469–90.
- 487 [3] Deri MA, Zeglis BM, Francesconi LC, Lewis JS. PET imaging with ^{89}Zr : From radiochemistry
488 to the clinic. *Nucl Med Biol* 2013;40:3–14.
- 489 [4] Zhang Y, Hong H, Cai W. PET tracers based on zirconium-89. *Curr Radiopharm*
490 2011;4:131–9.
- 491 [5] Severin GW, Engle JW, Barnhart TE, Nickles RJ. ^{89}Zr radiochemistry for positron emission
492 tomography. *Med Chem* 2011;7:389–94.
- 493 [6] Chang AJ, Desilva R, Jain S, Lears K, Rogers B, Lapi S. ^{89}Zr -radiolabeled trastuzumab
494 imaging in orthotopic and metastatic breast tumors. *Pharmaceuticals* 2012;5:79–93.
- 495 [7] Van Rij CM, Sharkey RM, Goldenberg DM, Frielink C, Molkenboer JDM, Franssen GM, et
496 al. Imaging of prostate cancer with immuno-PET and immuno-SPECT using a radiolabeled
497 anti-EGP-1 monoclonal antibody. *J Nucl Med* 2011;52:1601–7.
- 498 [8] Holland JP, Divilov V, Bander NH, Smith-Jones PM, Larson SM, Lewis JS. ^{89}Zr -DFO-J591 for
499 immunoPET of prostate-specific membrane antigen expression in vivo. *J Nucl Med*
500 2010;51:1293–300.
- 501 [9] Abou DS, Ku T, Smith-Jones PM. In vivo biodistribution and accumulation of ^{89}Zr in mice.
502 *Nucl Med Biol* 2011;38:675–81.
- 503 [10] Weiner R. The mechanism of ^{67}Ga localization in malignant disease. *Nucl Med Biol*
504 1996;23:745–51.
- 505 [11] Jørgensen JT, Persson M, Madsen J, Kjær A. High tumor uptake of ^{64}Cu : implications for
506 molecular imaging of tumor characteristics with copper-based PET tracers. *Nucl Med Biol*
507 2013;40:345–50.
- 508 [12] Sotogaku N, Endo K, Hirunuma R, Enomoto S, Ambe S, Ambe F. Biochemical reactions of
509 various trace elements with blood components and transport proteins. *J Radioanal Nucl*
510 *Chem* 1999;239:429–32.

- 511 [13] Bal W, Sokołowska M, Kurowska E, Faller P. Binding of transition metal ions to albumin:
512 sites, affinities and rates. *Biochim Biophys Acta* 2013;1830:5444–55.
- 513 [14] Heneweer C, Holland JP, Divilov V, Carlin S, Lewis JS. Magnitude of enhanced
514 permeability and retention effect in tumors with different phenotypes: ^{89}Zr -albumin as a
515 model system. *J Nucl Med* 2011;52:625–33.
- 516 [15] Matsumura Y, Maeda H. A new concept for macromolecular therapeutics in cancer
517 chemotherapy: Mechanism of tumorotropic accumulation of proteins and the antitumor
518 agent Smancs. *Cancer Res* 1986;46:6387–92.
- 519 [16] Schrettl M, Bignell E, Kragl C, Sabiha Y, Loss O, Eisendle M, et al. Distinct roles for intra-
520 and extracellular siderophores during *Aspergillus fumigatus* infection. *PLoS Pathog*
521 2007;3:1195–207.
- 522 [17] Petrik M, Haas H, Dobrozemsky G, Lass-Flörl C, Helbok A, Blatzer M, et al. ^{68}Ga -
523 siderophores for PET imaging of invasive pulmonary aspergillosis: proof of principle. *J*
524 *Nucl Med* 2010;51:639–45.
- 525 [18] Petrik M, Franssen GM, Haas H, Laverman P, Hörtnagl C, Schrettl M, et al. Preclinical
526 evaluation of two ^{68}Ga -siderophores as potential radiopharmaceuticals for *Aspergillus*
527 *fumigatus* infection imaging. *Eur J Nucl Med Mol Imaging* 2012;39:1175–83.
- 528 [19] Chiani M, Akbarzadeh A. Production of desferrioxamine B (Desferal) using corn steep
529 liquor in *Streptomyces pilosus*. *Pak J Biol Sci* 2010;13:1151–5.
- 530 [20] Holland JP, Sheh Y, Lewis JS. Standardized methods for the production of high specific-
531 activity zirconium-89. *Nucl Med Biol* 2009;36:729–39.
- 532 [21] Bruns S, Kniemeyer O, Hasenberg M, Amanianda V, Nietzsche S, Thywissen A, et al.
533 Production of extracellular traps against *Aspergillus fumigatus* in vitro and in infected
534 lung tissue is dependent on invading neutrophils and influenced by hydrophobin RodA.
535 *PLoS Pathog* 2010;6:e1000873.
- 536 [22] Kobayashi T, Sasaki T, Takagi I, Moriyama H. Zirconium solubility in ternary aqueous
537 system of Zr(IV)-OH-carboxylates. *J Nucl Sci Technol* 2009;46:142–8.
- 538 [23] Guérard F, Lee Y-S, Tripier R, Szajek LP, Deschamps JR, Brechbiel MW. Investigation of
539 Zr(IV) and ^{89}Zr (IV) complexation with hydroxamates: Progress towards designing a better
540 chelator than desferrioxamine B for immuno-PET imaging. *Chem Commun*
541 2013;49:1002–4.
- 542 [24] Holland JP, Evans MJ, Rice SL, Wongvipat J, Sawyers CL, Lewis JS. Annotating MYC status
543 with ^{89}Zr -transferrin imaging. *Nat Med* 2012;18:1586–91.

- 544 [25] Gotthardt M, Bleeker-Rovers CP, Boerman OC, Oyen WJG. Imaging of inflammation by
545 PET, conventional scintigraphy, and other imaging techniques. *J Nucl Med Technol*
546 2013;41:157–69.
- 547 [26] Vavere AL, Welch MJ. Preparation, biodistribution, and small animal PET of ⁴⁵Ti-
548 transferrin. *J Nucl Med* 2005;46:683–90.
- 549 [27] Jensen AI, Binderup T, Kumar EK P, Kjær A, Rasmussen PH, Andresen TL. Positron
550 emission tomography based analysis of long-circulating cross-linked triblock polymeric
551 micelles in a U87MG mouse xenograft model and comparison of DOTA and CB-TE2A as
552 chelators of copper-64. *Biomacromolecules* 2014;15:1625–33.
- 553 [28] Petersen AL, Binderup T, Rasmussen P, Henriksen JR, Elema DR, Kjær A, et al. ⁶⁴Cu loaded
554 liposomes as positron emission tomography imaging agents. *Biomaterials* 2011;32:2334–
555 41.
- 556 [29] Abou DS, Thorek DLJ, Ramos NN, Pinkse MWH, Wolterbeek HT, Carlin SD, et al. ⁸⁹Zr-
557 labeled paramagnetic octreotide-liposomes for PET-MR imaging of cancer. *Pharm Res*
558 2013;30:878–88.
- 559 [30] Harrington KJ, Syrigos KN, Uster PS, Abra RM, Stewart JSW. Biodistribution and
560 pharmacokinetics of In-DTPA-labelled pegylated liposomes in a human tumour xenograft
561 model : implications for novel targeting strategies. *Br J Cancer* 2000;83:232–8.
- 562 [31] Harrington KJ, Mohammadtaghi S, Uster PS, Harrington KJ, Mohammadtaghi S, Uster PS,
563 et al. Effective targeting of solid tumors in patients with locally advanced cancers by
564 radiolabeled pegylated liposomes effective targeting of solid tumors in patients with
565 locally advanced cancers by radiolabeled pegylated liposomes. *Clin Cancer Res*
566 2001:243–54.
- 567 [32] Verel I, Visser GWM, van Dongen GAMS. The promise of immuno-PET in
568 radioimmunotherapy. *J Nucl Med* 2005;46 Suppl 1:164S–71S.
- 569 [33] Börjesson PKE, Jauw YWS, de Bree R, Roos JC, Castelijns JA, Leemans CR, et al. Radiation
570 dosimetry of ⁸⁹Zr-labeled chimeric monoclonal antibody U36 as used for immuno-PET in
571 head and neck cancer patients. *J Nucl Med* 2009;50:1828–36.

572

573

574 **Table 1.** pH ranges of ^{89}Zr complex preparations as measured after 10 minutes of mixing of ^{89}Zr
 575 chloride with the corresponding solution.

Mixture	pH range
Oxalate 5.5	4.87 – 6.01
Oxalate 7.0	6.74 – 7.45
Citrate 5.5	5.43 – 5.58
Citrate 7.0	6.60 – 6.93
Sucrose	5.12 – 6.77
Acetate 5.5	5.51 – 5.52
Acetate 7.0	6.43 – 7.54
Chloride	4.99 – 5.68
Water	4.65 – 4.95

576

577

578 **Table 2.** Biodistribution of ^{89}Zr , injected as the oxalate, in tumor-bearing mice. Averages and
 579 standard deviations are given (n = 3 for FaDu, n = 4 for HT29). Animals were injected
 580 intravenously with ^{89}Zr oxalate and imaged for up to 68 h. Tumor levels were higher than muscle
 581 at all measurement points. Tumor levels were higher than blood (heart) after 45 h. Errors indicate
 582 one standard deviation. 9-15 MBq was administered to each mouse, 10 min scans were acquired

		%ID/g (\pm SD)						
	Xenograft	Heart	Kidney	Bladder	Liver	Tumor	Muscle	Bone
	All (n = 7)	10.59 (\pm 2.47)	4.69 (\pm 1.21)	4.04 (\pm 2.91)	6.07 (\pm 1.92)	2.99 (\pm 0.35)	1.98 (\pm 0.31)	4.30 (\pm 1.08)
1h	FaDu	11.83 (\pm 3.01)	5.55 (\pm 1.45)	2.93 (\pm 1.00)	7.40 (\pm 2.26)	2.97 (\pm 0.37)	2.03 (\pm 0.42)	4.53 (\pm 1.66)
	HT29	9.65 (\pm 1.84)	4.05 (\pm 0.48)	4.88(\pm 3.76)	5.08 (\pm 0.93)	3.00 (\pm 0.36)	1.94 (\pm 0.26)	4.13 (\pm 0.64)

	All (n = 7)	5.31 (± 2.42)	2.56 (± 1.09)	3.26 (± 0.91)	3.36 (± 1.69)	3.46 (± 0.65)	1.76 (± 0.46)	9.04 (± 2.59)
6h	FaDu	6.53 (± 2.95)	3.25 (± 1.31)	3.23 (± 1.46)	4.37 (± 2.02)	4.08 (± 0.41)	2.05 (± 0.55)	10.37 (± 3.58)
	HT29	4.40 (± 1.81)	2.04 (± 0.61)	3.28 (± 0.48)	2.60 (± 1.09)	2.99 (± 0.29)	1.54 (± 0.25)	8.05 (± 1.35)
	All (n = 7)	1.86 (± 1.49)	1.35 (± 0.68)	1.05 (± 0.28)	1.77 (± 1.33)	2.99 (± 1.22)	0.99 (± 0.40)	12.76 (± 2.24)
20h	FaDu	3.07 (± 1.47)	1.85 (± 0.77)	1.15 (± 0.34)	2.77 (± 1.46)	4.13 (± 0.96)	1.37 (± 0.23)	13.63 (± 1.56)
	HT29	0.95 (± 0.65)	0.97 (± 0.31)	0.97 (± 0.25)	1.03 (± 0.60)	2.14 (± 0.40)	0.71 (± 0.18)	12.10 (± 2.65)
	All (n = 7)	0.67 (± 0.56)	0.91 (± 0.44)	0.60 (± 0.22)	1.39 (± 0.99)	2.47 (± 0.95)	0.76 (± 0.36)	14.89 (± 1.32)
45h	FaDu	1.09 (± 0.67)	1.24 (± 0.53)	0.72 (± 0.32)	2.14 (± 1.19)	3.27 (± 0.97)	1.07 (± 0.36)	13.17 (± 0.78)
	HT29	0.35 (± 0.09)	0.66 (± 0.10)	0.50 (± 0.04)	0.83 (± 0.26)	1.88 (± 0.23)	0.53 (± 0.10)	15.58 (± 1.25)
	All (n = 7)	0.55 (± 0.31)	0.86 (± 0.32)	0.50 (± 0.08)	1.30 (± 0.82)	2.05 (± 0.76)	0.65 (± 0.29)	12.99 (± 1.45)
68h	FaDu	0.86 (± 0.14)	1.00 (± 0.40)	0.54 (± 0.08)	1.93 (± 0.92)	2.72 (± 0.74)	0.78 (± 0.37)	13.77 (± 0.32)
	HT29	0.32 (± 0.06)	0.75 (± 0.24)	0.48 (± 0.07)	0.82 (± 0.27)	1.55 (± 0.13)	0.56 (± 0.20)	12.41 (± 1.75)

583

584

585

586 **Table 3.** *Ex vivo* biodistribution of organs of naïve (n = 4) and infected mice (n = 4). The mice
587 were infected with *A. fumigatus* and after 21 hours of disease progression, they were injected
588 with 10-12 MBq ⁸⁹Zr oxalate. Tissues were excised and measured three hours after the injection.
589 Data are %ID/g, expressed as the mean or as lung-to-muscle ratios ± 1 SD. Significantly
590 different organs are shown in bold with * (p < 0.05) or ** (p < 0.01).

Organ	Naïve mice	Infected mice
Blood	10.5 (± 2.7)	8.6 (± 2.8)
Lung**	6.0 (± 1.1)	11.6 (± 1.8)
Muscle	1.6 (± 0.5)	1.9 (± 0.2)
Liver	4.0 (± 0.8)	3.3 (± 0.7)
Heart	5.8 (± 2.2)	5.6 (± 1.5)
Kidney	6.1 (± 1.5)	8.3 (± 1.6)

Stomach*	2.5 (± 0.2)	3.5 (± 0.7)
Colon*	2.6 (± 0.4)	3.5 (± 0.2)
Brain	0.5 (± 0.1)	0.5 (± 0.1)
Spine*	5.0 (± 0.9)	3.8 (± 0.4)
Femur right	9.9 (± 4.3)	6.6 (± 0.5)
Femur left	9.0 (± 3.5)	6.5 (± 1.3)
Lung/muscle	3.8 (± 2.3)	6.3 (± 7.7)

591

592

593

594

595

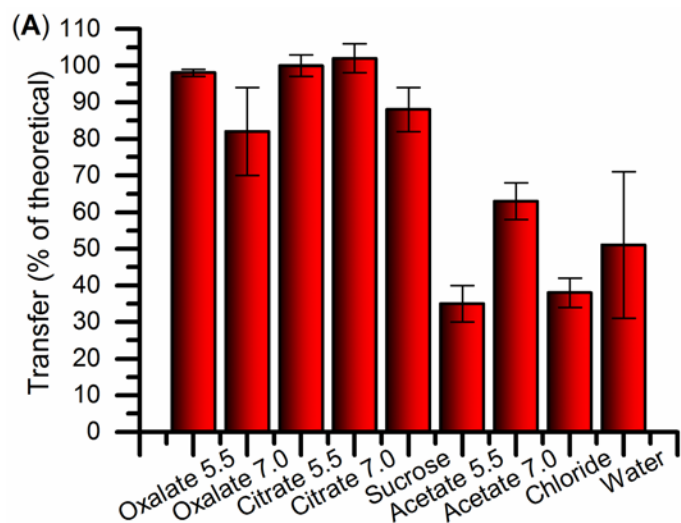
596

597

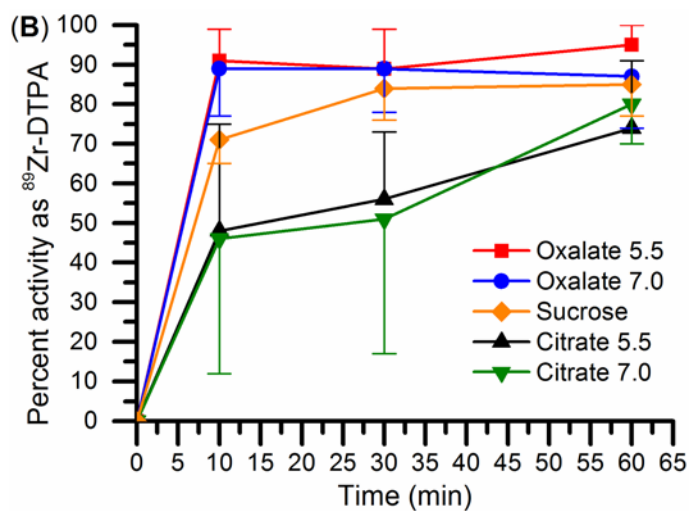
598

599

600



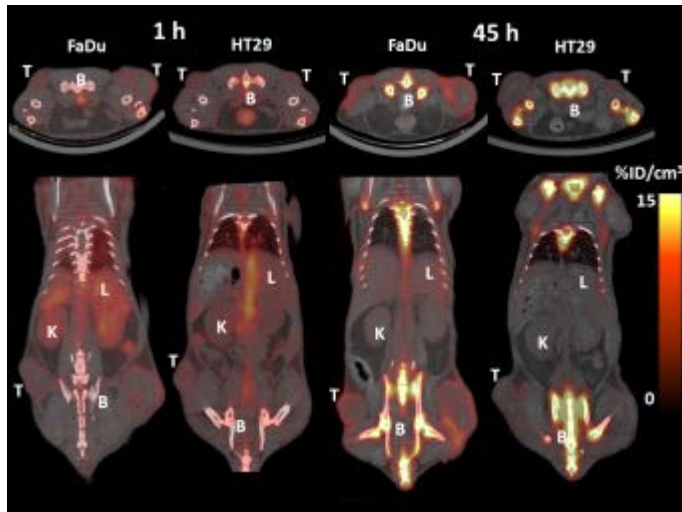
601



602

603 **Figure 1.** (A) Transferability/dissolution of ⁸⁹Zr mixtures. The y-axis shows transferability as the
 604 activity in a removed aliquot of 300 μL compared to the theoretical maximum activity removed
 605 from a homogeneous solution, as calculated by the equation $transferability = A_{300\mu L} * (1.3/0.3) /$
 606 $A_{1300\mu L} * 100\%$. n = 3 in all cases, error bars show one standard deviation. (B) Transchelation of
 607 ⁸⁹Zr mixtures to DTPA. Oxalate at both pH values showed fast transchelation, reaching about
 608 90% after 10 minutes, while sucrose and especially the citrates showed a slower shift of the
 609 radioactivity to DTPA. n = 3 in all cases, error bars showing one standard deviation are one-
 610 sided to improve legibility.

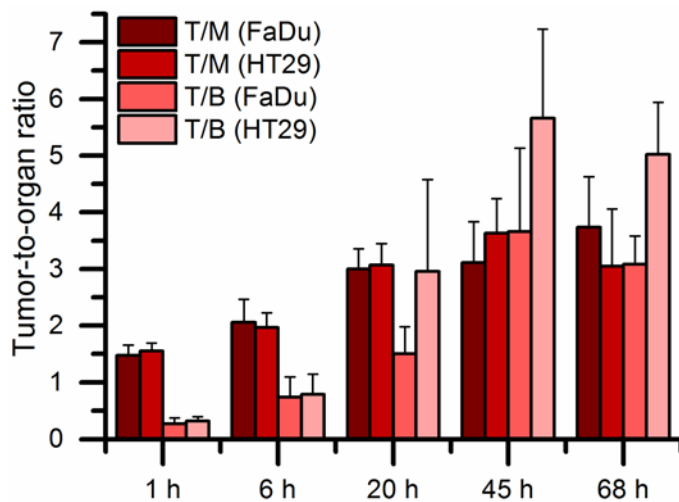
611



612

613 **Figure 2.** Representative transverse (top lane) and coronal (bottom lane) images of ^{89}Zr -
 614 distribution in FaDu and HT29 tumor bearing animals acquired by ten minute static PET scans, 1
 615 h (left) and 45 h (right) after tracer administration (FaDu: 12.47 MBq injected, HT29: 9.40 MBq
 616 injected). Animals were sedated with sevoflurane. White letters on images marks T: tumor; B:
 617 bone; L: liver and K: kidney.

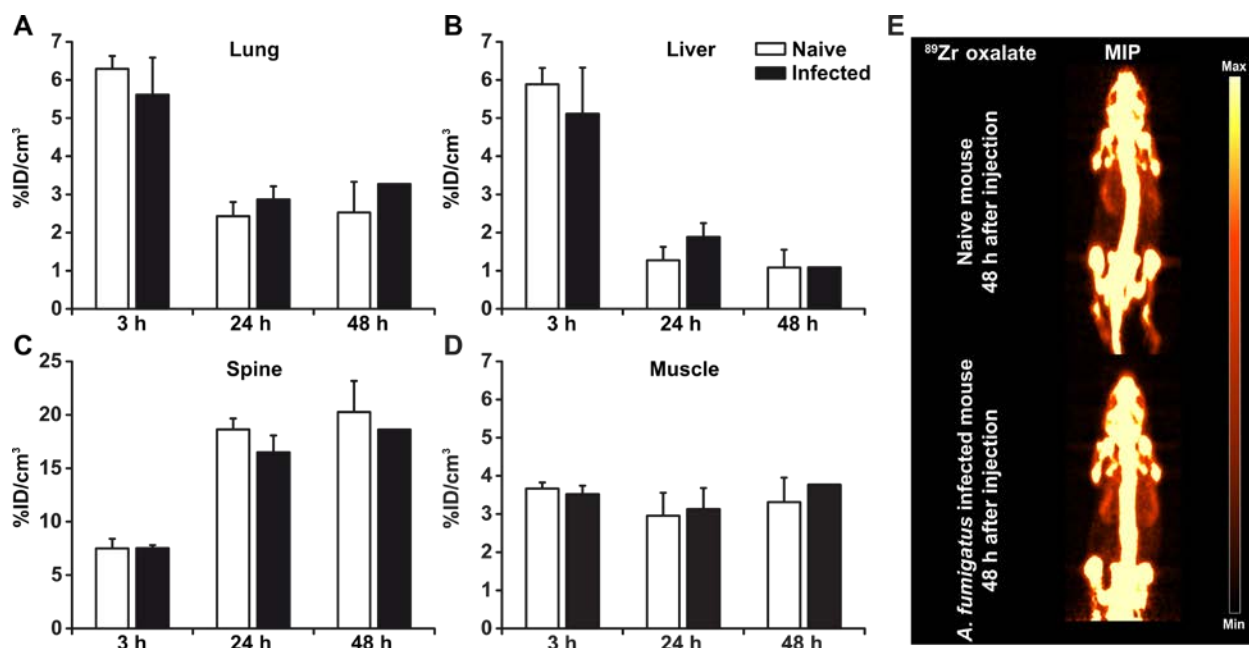
618



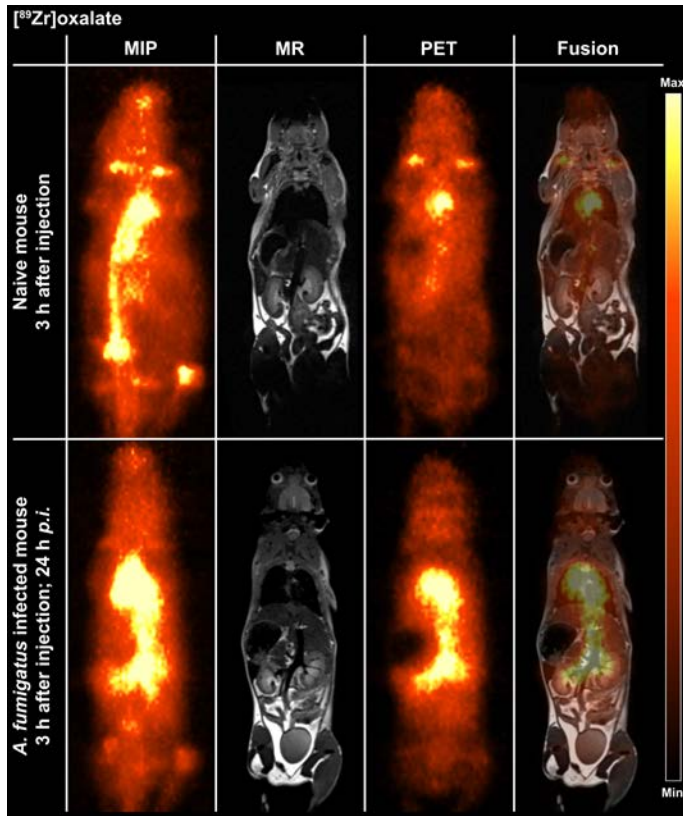
619

620 **Figure 3.** Tumor-to-muscle (T/M) and tumor-to-blood (T/B) ratios of injected ^{89}Zr oxalate in
 621 mice bearing FaDu or HT29 tumor xenografts. The blood values are taken as $\%ID/cm^3$ of the
 622 heart. The T/M values for both tumor types are seen to rise until 20 h and subsequently stabilize

623 between 3.0-3.7 for both tumors. T/B values for both tumor types increase until 45 h. Error bars
 624 indicate one standard deviation. n = 3 (FaDu), n = 4 (HT29). 9-15 MBq was administered to each
 625 mouse, 10 min scans were acquired.
 626

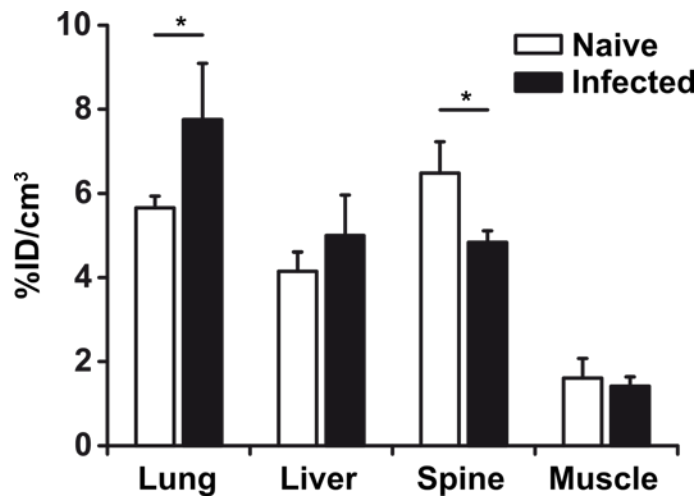


627
 628 **Figure 4 (A)-(D).** PET quantification (%ID/cm³) of organs of naïve and infected mice 3 h, 24 h,
 629 48 h post injection of ⁸⁹Zr oxalate. (E) Maximum intensity projection (MIP) of a naïve and an
 630 infected mouse at the 48 h time-point, demonstrating the high uptake of ⁸⁹Zr in the bones.
 631 Injected radioactivity was between 10 and 12 MBq. The mice were sedated with isoflurane and
 632 scanned for 10 minutes. Data are given as %ID/cm³ ± 1 SD.



633

634 **Figure 5.** Maximum intensity projections (MIP) of PET and fused PET and MR images of naïve
 635 or neutropenic *A. fumigatus* infected mice. The PET/MR imaging was done three hours after
 636 injection with ^{89}Zr oxalate and 21 hours post infection (p.i.) of the mice with *A. fumigatus*.
 637 Perfusion effects and thereby enhanced ^{89}Zr oxalate accumulation is seen in the lungs of the *A.*
 638 *fumigatus* infected mouse as depicted in the lower lane. The mice were sedated with isoflurane
 639 and scanned for 10 minutes. Injected radioactivity was between 10 and 12 MBq



640

641 **Figure 6.** PET quantification (%ID/cm³) of tissue ROIs from naïve and infected mice with
 642 advanced disease. The data were taken 24 h post-infection, and 3 h after injection of ⁸⁹Zr oxalate.

643 Data are given as %ID/cm³ ± 1 SD. *Tissues are considered statistically significant, with p<0.05.

644

645